

**Bianchi I effective dynamics in quantum reduced loop gravity**Emanuele Alesci,<sup>1</sup> Gioele Botta,<sup>2</sup> Giovanni Luzi,<sup>3</sup> and Gabriele V. Stagno<sup>4,5</sup><sup>1</sup>*Institute for Gravitation and the Cosmos, Penn State, University Park, Pennsylvania 16802, USA*<sup>2</sup>*Faculty of physics, University of Warsaw, Pasteura 5, 02-093 Warsaw, Poland*<sup>3</sup>*LSTME Busan Branch, 1276 Jisa-Dong, Gangseo-Gu, Busan 46742, Republic of Korea*<sup>4</sup>*Sapienza University of Rome, P.le Aldo Moro 5, (00185) Roma, Italy*<sup>5</sup>*Aix Marseille Univ., Univ. de Toulon, CNRS, CPT, UMR 7332, 13288 Marseille, France*

(Received 25 February 2019; published 20 May 2019)

The effective quantum dynamics of Bianchi I spacetime is addressed within the statistical regularization scheme in quantum reduced loop gravity. The case of a minimally coupled massless scalar field is studied and compared with the effective  $\bar{\mu}$ -loop quantum cosmology. The dynamics provided by the two approaches match in the semiclassical limit but differ significantly after the bounces. Analytical and numerical inspections show that energy density, expansion scalar and shear are bounded also in quantum reduced loop gravity and the classical singularity is resolved for generic initial conditions in all spatial directions.

DOI: [10.1103/PhysRevD.99.106009](https://doi.org/10.1103/PhysRevD.99.106009)**I. INTRODUCTION**

Quantum reduced loop gravity (QRLG) [1,2] is aimed to address symmetric sectors of loop quantum gravity (LQG) [3,4] and it has proved to be a versatile and powerful tool for both primordial cosmology [5,6] and black hole physics [7]. It is based on suitable gauge fixings of LQG (see e.g., [8]) and reduces the computational tasks that plague the full theory whilst retaining its main features—graph and intertwiner structure—allowing a deeper theoretical understanding [9,10] and the actual computation of observational consequences [11].

QRLG has been originally designed for dealing with cosmology, and here it has been successful in bridging loop quantum cosmology (LQC) (see [12] for a recent review) to full LQG [10,13]. From the QRLG perspective, LQC stands as a first order effective quantization that can be refined within QRLG including key quantum terms coming from the full theory. Those corrections are crucial and they must be taken into account when one is interested in questioning the deep quantum regime of the universe. For instance, for the Friedmann Lemaitre Robertson Walker (FLRW) model they provide a quantum evolution which significantly differs from the one given by LQC: the big bounce scenario provided by the former [14] is replaced in QRLG by the dynamics of an emergent-bouncing universe [5]. The universe “emerges” from an infinite past with a nonvanishing volume that it keeps until a transient phase of expansions and contractions occurs and eventually matches the LQC evolution. This alternative cosmology has been recently considered also in different contexts (see [15] and references there in) and its observational signatures have been studied in [16], and by some of the authors in [11,17].

Going beyond the isotropic context is a needed step both for testing the QRLG approach in a more general setting and for addressing the issue of isotropization (e.g., see [18]), a mechanism that is believed to have a quantum origin and to be responsible for the observed large scale symmetry of our universe. The issue of anisotropy has already been faced by many works in LQC [19–23] where it has revealed to be less trivial than what was initially expected. As for the isotropic context, the quantization deeply depends on the chosen regularization scheme for the classical symmetry reduced Hamiltonian constraint. The obvious generalization of the  $\mu_0$ -scheme [24] adopted for the FLRW quantization, leads to unwanted features such as a singularity resolution that can be tuned to be at any value of the energy density, i.e., even way less than Planckian values. This issue was finally fixed choosing a different regularization scheme [25] that is a generalization of the  $\bar{\mu}$ -scheme implemented in FLRW [14]. In this paper we study the homogeneous anisotropic sector of QRLG associated to the Bianchi I geometry, within the statistical regularization scheme [6]. This framework provides an effective graph-changing dynamics for both isotropic and nonisotropic sectors and includes LQC regularizations as special cases. From the LQC perspective, the QRLG statistical regularization places itself between the aforementioned  $\mu_0$  and  $\bar{\mu}$ -scheme, as explained in [6]. In addition, it provides a dynamics for states living on the kinematical arena defined by gauge fixing the full LQG to diagonal triads and metrics.<sup>1</sup> An effective Hamiltonian for the (quantum corrected) geometry of the Bianchi I universe

<sup>1</sup>For a similar approach see also [26].

is considered by taking the expectation value of the (reduced) nongraph-changing Hamiltonian operator over a Gaussian ensemble of coherent states peaked on classical Bianchi I phase-space and based on cuboidal graphs with different number of nodes  $A_i$ . For large  $A_i$ , one can expand the integral over the ensemble that defines the QRLG-effective Hamiltonian, finding a zero order contribution which coincides with the standard LQC Bianchi I effective Hamiltonian plus (infinitely many) corrections that become relevant in the deep quantum era [6]. Here we have addressed the dynamics of the QRLG model considering all those contributions, i.e., without approximating the integral to a given order, and made a comparison with the dynamics provided by the standard effective LQC in the presence of a massless scalar field  $\phi$ . The usual Hamilton equations are used to obtain the associated effective dynamics and the evolution is numerically studied for some general initial conditions, i.e., isotropic, “Kasner-like” (one direction expands/contracts and the other two contract/expand) and “un-Kasner like” (all directions expand/contract). Similarly to what happens in the isotropic case,<sup>2</sup> the QRLG-quantum corrections to the classical Bianchi I model provide a non singular dynamics that significantly differs from the one given by LQC before the bounces and matches it afterwards. More specifically, the QRLG model turns out not to bridge two classical Bianchi I universes, as instead it occurs in LQC [27]. Starting from a classical Bianchi I and going backward in the relational time  $\phi$ , the universe undergoes three bounces (one in each direction) and after that its scale factors start growing faster than they do in LQC and GR. Moreover, our numerical simulations show that the singularity is avoided in all directions for generic initial conditions. In particular, for Kasner-like initial conditions each directional scale factor is nonvanishing, contrary to what happens in the LQC-evolution where one of the scale factor goes to zero in the far past [27].

The paper is organized as follows. We start recalling useful definitions for the Bianchi I geometry and its Hamiltonian formulation in terms of the Ashtekar variables. The relevant kinematical quantities, such as the directional Hubble rates, the expansion scalar and the shear are then introduced. In Sec. III the Hamiltonian constraints for the Bianchi I model are given for both GR and LQC. The QRLG-Bianchi I model is defined in Sec. IV and the expressions of the kinematical quantities, defined in general terms in Sec. II, are here given explicitly for our QRLG-model. Analytical bounds for those quantities and for the energy density are computed and their evolutions numerically studied in Sec. VI. Section V presents the numerical study of the QRLG-Bianchi I effective dynamics for the minimally coupled massless scalar field, compared to the

one provided by the LQC. Finally, the last section is devoted to conclusions and outlooks.

Throughout the paper we use  $\gamma = 0.24$  and  $G = \hbar = c = 1$ , so that  $l_p^2 := \hbar G/c^3 = 1$ . We do not follow Einstein notation, i.e., repeated indices are not summed over, except where explicitly stated otherwise.

## II. BIANCHI I GEOMETRY AND RELATED KEY QUANTITIES

We review here some useful definitions for the Bianchi I model in the Ashtekar variables. Everything in this section holds for GR, effective LQC and effective QRLG.

### A. Line element

We choose cartesian comoving coordinates  $(t, x^b)$  and unitary lapse function. The Bianchi I geometry is then associated to the following line element:

$$ds^2 = -dt^2 + \sum_{bc} q_{bc}(t) dx^b dx^c = -dt^2 + \sum_b (a_b(t) dx^b)^2, \quad (1)$$

where  $a_b(t)$  are the scale factors for the spatial directions  $b = 1, 2, 3$ .

### B. Symplectic structure

The Hamiltonian formulation of the geometry (1) closely follows the one implemented for the FLRW case [24]. Once a fiducial *cuboidal* cell  $\mathcal{V}$  of coordinate sides  $\tilde{L}^i$  is introduced, a parametrization of the phase-space associated to the geometry is provided by the Ashtekar variables, i.e., by the connection  $A_a^i(t)$  and the densitized triad  $E_i^a(t)$  [25]:

$$A_a^i(t) := \frac{c^i(t)}{\tilde{L}^i} \tilde{e}_a^i, \quad E_i^a(t) := \frac{p_i(t)}{\tilde{V}} \tilde{L}^i \tilde{e}_i^a, \quad (2)$$

where  $\tilde{e}_a^i = \delta_a^i$  and  $\tilde{e}_i^a = \delta_i^a$  are, respectively, the orthonormal flat fiducial cotriad and triad field adapted to  $\mathcal{V}$ ,

$$q_{bc} = \sum_{ik} a_b \tilde{e}_b^i a_c \tilde{e}_c^k \delta_{ik},$$

and  $\tilde{L}^j$  are the set of coordinate lengths defining the coordinate volume  $\tilde{V} = \tilde{L}^1 \tilde{L}^2 \tilde{L}^3$  of the fiducial cell, which is related to the physical volume<sup>3</sup>  $V$  as

$$V = a_1 a_2 a_3 \tilde{V} = \sqrt{p_1 p_2 p_3}. \quad (3)$$

Connections and triads are diagonal matrices whose entries satisfy the following Poisson bracket:

<sup>2</sup>For both the “volume counting” [5] and “area counting” [6] statistical regularizations.

<sup>3</sup>In QRLG this quantity is taken to be the volume of the biggest observable region of the universe, as explained in [6].

$$\{c^i, p_j\} = 8\pi\gamma\delta_j^i, \quad (4)$$

which defines the symplectic structure for the geometrical sector of the model. The  $p_j$  are related to the scale factors  $a_k$  as follows (we choose a positive orientation)

$$p_i = \tilde{L}^j \tilde{L}^k |a_j a_k| \quad i = 1, 2, 3 \quad i \neq j \neq k. \quad (5)$$

Finally, when the geometry is sourced by a scalar field, the phase-space gets enlarged and coordinatized by the 8-tuples  $(c^i, p_i, \phi, p_\phi)$ , where

$$\{\phi, p_\phi\} = 1. \quad (6)$$

### C. Dynamics and energy density

Hereafter we will refer to the case of the Bianchi I geometry filled with a massless scalar field  $\phi$ .

The dynamics is generated by the following Hamiltonian constraint:

$$\mathcal{C}(c^i, p_i, p_\phi) := H_{BI}(c^i, p_i) + H_\phi(p_\phi, p_i) \approx 0, \quad (7)$$

where  $H_{BI} := H_{gr}, H_{lqc}, H$  generically refers to the geometrical sector in GR, LQC and QRLG, respectively (for their actual definitions see the following sections), and

$$H_\phi := \frac{p_\phi^2}{2V}, \quad (8)$$

is the kinetic energy of the field  $\phi$ , the only contribution coming from the matter sector. The Hamilton's equations follow:

$$\begin{aligned} \dot{c}^i &= 8\pi\gamma \frac{\partial \mathcal{C}}{\partial p_i}, & \dot{p}_i &= -8\pi\gamma \frac{\partial \mathcal{C}}{\partial c^i}, \\ \dot{\phi} &= \frac{\partial H_\phi}{\partial p_\phi}, & \dot{p}_\phi &= -\frac{\partial H_\phi}{\partial \phi}. \end{aligned} \quad (9)$$

Soon we will be interested in evaluating the field energy density  $\rho$  along the physical motions. It is given by the ratio

$$\rho := \frac{H_\phi}{V} \approx -\frac{H_{BI}}{\sqrt{p_1 p_2 p_3}}. \quad (10)$$

### D. Directional Hubble rates, expansion scalar and shear

The main kinematical quantities are the directional Hubble rates  $H_i := \dot{a}_i/a_i$ . In terms of the triads (5) they read

$$H_i = \frac{1}{2} \left( -\frac{\dot{p}_i}{p_i} + \frac{\dot{p}_j}{p_j} + \frac{\dot{p}_k}{p_k} \right) \quad i = 1, 2, 3, \quad i \neq j \neq k, \quad (11)$$

and from them two more useful quantities are built: the expansion scalar  $\theta$ ,

$$\theta := \frac{1}{V} \frac{dV}{dt} = \sum_i H_i, \quad (12)$$

and the shear  $\sigma^2$ ,

$$\begin{aligned} \sigma^2 &:= \sum_i H_i^2 - \frac{\theta^2}{3} \\ &= \frac{1}{3} [(H_1 - H_2)^2 + (H_2 - H_3)^2 + (H_3 - H_1)^2], \end{aligned} \quad (13)$$

which clearly vanishes in the isotropic limit.

## III. CLASSICAL AND EFFECTIVE-LQC CONSTRAINTS FOR BIANCHI I

In the following sections we will compare the dynamics of the QRLG model to the one provided by LQC. For this purpose and in order to understand the choice of the initial conditions for the dynamical problem, we recall here the Hamiltonian constraints for the Bianchi I geometry in GR and LQC.

The classical Bianchi I universe is associated to the constraint<sup>4</sup>  $\mathcal{C}_{gr}$ ,

$$\begin{aligned} \mathcal{C}_{gr} &:= H_{gr} + H_\phi \\ &:= -\frac{1}{8\pi\gamma^2} \frac{(c_2 p_2 c_3 p_3 + c_1 p_1 c_3 p_3 + c_1 p_1 c_2 p_2)}{\sqrt{p_1 p_2 p_3}} \\ &\quad + \frac{p_\phi^2}{2\sqrt{p_1 p_2 p_3}} \approx 0, \end{aligned} \quad (14)$$

where the  $p_i$  follow from the general definition (5) and the connections are proportional to the directional Hubble rates:

$$c_i = \gamma L_i H_i, \quad (15)$$

being  $L_i := a_i \tilde{L}_i$ . Note that (15) strictly holds in GR and it is only approximately true in LQC and QRLG in the classical limit  $p_i \gg 1$ ,  $c_i \ll 1$ , where we will choose the initial conditions for the dynamical problem for both LQC and QRLG (see below).

The effective  $\bar{\mu}$ -LQC of Bianchi I is obtained [25,27] by replacing the classical connections in (14) according to the ‘‘polymeric prescription’’, i.e.,:

$$c_i \rightarrow \frac{\sin(\bar{\mu}_i c_i)}{\bar{\mu}_i} \quad (16)$$

<sup>4</sup>Hereafter we will deliberately loose track of covariance/contravariance using only downstairs indices.

where

$$\bar{\mu}_i := \sqrt{\Delta_{\text{LQG}}} \sqrt{\frac{p_i}{p_j p_k}} \quad i \neq j \neq k \quad (17)$$

and  $\Delta_{\text{LQG}} = 5.22$  is the LQG area gap. The resulting effective constraint  $\mathcal{C}_{\text{lqc}}$  reads<sup>5</sup>:

$$\begin{aligned} \mathcal{C}_{\text{lqc}} &:= H_{\text{lqc}} + H_\phi \\ &:= -\frac{1}{8\pi\gamma^2 \sqrt{p_1 p_2 p_3}} \left( \frac{\sin(\bar{\mu}_2 c_2) \sin(\bar{\mu}_3 c_3)}{\bar{\mu}_2 \bar{\mu}_3} p_2 p_3 \right. \\ &\quad \left. + \text{cyclic terms} \right) + \frac{p_\phi^2}{2\sqrt{p_1 p_2 p_3}} \approx 0. \end{aligned} \quad (18)$$

#### IV. THE QRLG-BIANCHI I MODEL

The effective Hamiltonian we introduce here is the one provided by QRLG within the ‘‘area counting’’ statistical regularization scheme [6]. Its expression is given by the expectation value of the (reduced) scalar constraint  $\hat{H}^R$  over a classical mixture of coherent states based on cuboidal graphs with different number of nodes  $A_i$ . The mixture is described by the following density matrix:

$$\hat{\rho}_A := \prod_i \sum_{A_i=1}^{A_i^{\max}} \binom{A_i^{\max}}{A_i} |A_i, j_i, \theta_i\rangle \langle A_i, j_i, \theta_i|, \quad (19)$$

where  $|A_i, j_i, \theta_i\rangle$  are the Thiemann’s coherent states in the kinematical space of QRLG [9], peaked on both the intrinsic and extrinsic geometry of the classical Bianchi I, i.e., on the QRLG fluxes  $E_i = 8\pi\gamma l_p^2 j_i$  and holonomies  $h_i = e^{i\theta_i l_i}$ . The maximum number of nodes contained in the physical area  $p_i$  is

$$A_i^{\max} = \frac{2p_i}{\Delta'} \quad (20)$$

where  $\Delta' = 6.03$  is the ‘‘area counting’’ area gap in QRLG<sup>6</sup> and the expectation value

$$H^{\text{disc}} := \frac{\text{Tr}(\hat{\rho}_A \hat{H}^R)}{\text{Tr} \hat{\rho}_A} \quad (21)$$

explicitly reads:

<sup>5</sup>We neglect holonomy corrections. Those are expected to be subleading for super-Planckian volumes, condition that is always met in our numerical simulations, see Sec. V.

<sup>6</sup>Which is slightly greater than the usual LQG-value  $\Delta_{\text{LQG}} = 5.22$ , as explained in [6].

$$\begin{aligned} H^{\text{disc}}(\{A_i^{\max}(p_i)\}, \{c_i\}) \\ = -\frac{1}{8\pi\gamma^2} \frac{\left[ \prod_i \sum_1^{A_i^{\max}} \binom{A_i^{\max}}{A_i} \right] \tilde{H}(\{A_i^{\max}(p_i)\}, \{c_i\}; \{A_i\})}{\prod_i \sum_1^{A_i^{\max}} \binom{A_i^{\max}}{A_i}}, \end{aligned} \quad (22)$$

where

$$\begin{aligned} \tilde{H} &:= A_1 \sqrt{\frac{p_2 p_3}{p_1}} \sin\left(c_2 \sqrt{\frac{A_2}{A_1 A_3}}\right) \sin\left(c_3 \sqrt{\frac{A_3}{A_1 A_2}}\right) \\ &\quad + \text{cyclic terms.} \end{aligned} \quad (23)$$

For  $A_i \gg 1$  we will use the continuous approximation<sup>7</sup> for the binomials considering the following expression

$$\begin{aligned} H(\{p_i\}, \{c_i\}) \\ := -\frac{1}{8\pi\gamma^2} \frac{\left[ \prod_i \int_1^{2p_i/\Delta'} e^{-\frac{\Delta'}{p_i}(A_i - \frac{p_i}{\Delta'})^2} dA_i \right] \tilde{H}(\{p_i\}, \{c_i\}; \{A_i\})}{\prod_i \int_1^{2p_i/\Delta'} e^{-\frac{\Delta'}{p_i}(A_i - \frac{p_i}{\Delta'})^2} dA_i}. \end{aligned} \quad (24)$$

as our Hamiltonian for the geometrical sector. Including the contribution of the matter sector, we find the total constraint

$$\mathcal{C}_{\text{qrlg}} := H + H_\phi \approx 0, \quad (25)$$

which completes the definition of our model.

#### A. $\rho$ , $\theta$ and $\sigma^2$ explicit expressions for the model

In this section we provide the explicit expressions for the phase-space functions (10), (12), (13) for the constraint (25). The analytical bounds and the numerical evolutions along physical motions for those quantities, are discussed in Sec. VI.

##### 1. Energy density

After a sign change, the ratio between (24) and the physical volume  $V$  gives the energy density

$$\begin{aligned} \rho(\{p_i\}, \{c_i\}) \\ = \frac{1}{8\pi\gamma^2 \sqrt{p_x p_y p_z}} \\ \times \frac{\left[ \prod_i \int_1^{2p_i/\Delta'} e^{-\frac{\Delta'}{p_i}(A_i - \frac{p_i}{\Delta'})^2} dA_i \right] \tilde{H}(\{p_i\}, \{c_i\}; \{A_i\})}{\prod_i \int_1^{2p_i/\Delta'} e^{-\frac{\Delta'}{p_i}(A_i - \frac{p_i}{\Delta'})^2} dA_i}. \end{aligned} \quad (26)$$

<sup>7</sup>Note that already for  $A_i > 12$  we have good agreement with the exact expression (22) (see Figs. 10 and 11), thus, in Sec. V the dynamics has been studied within the continuous approximation.

## 2. Expansion scalar

From the very definition (12) and the Hamilton's equations (9), the expansion scalar reads

$$\begin{aligned}\theta &= \frac{1}{\sqrt{p_1 p_2 p_3}} \frac{d\sqrt{p_1 p_2 p_3}}{dt} \\ &= -\frac{8\pi\gamma}{2} \sum_j \frac{1}{p_j} \frac{\partial \mathcal{C}}{\partial c_j} \\ &= -\frac{8\pi\gamma}{2} \sum_j \frac{1}{p_j} \frac{\partial H_{BI}}{\partial c_j},\end{aligned}\quad (27)$$

and for  $H_{BI} = H$  we obtain the actual expression for the QRLG model:

$$\theta = \frac{1}{2\gamma} \frac{\left[ \prod_i \int_1^{2p_i/\Delta'} e^{-\frac{\Delta'}{p_i}(A_i - \frac{p_i}{\Delta'})^2} dA_i \right] \sum_j \frac{1}{p_j} \frac{\partial \tilde{H}}{\partial c_j}(\{p_i\}, \{c_i\}; \{A_i\})}{\prod_i \int_1^{2p_i/\Delta'} e^{-\frac{\Delta'}{p_i}(A_i - \frac{p_i}{\Delta'})^2} dA_i}\quad (28)$$

where

$$\begin{aligned}\frac{1}{p_j} \frac{\partial \tilde{H}}{\partial c_j}(\{p_i\}, \{c_i\}; \{A_i\}) \\ = \sum_{i,k} \sqrt{\frac{p_k}{p_i p_j}} \sqrt{\frac{A_j A_i}{A_k}} \cos\left(c_j \sqrt{\frac{A_j}{A_i A_k}}\right) \sin\left(c_k \sqrt{\frac{A_k}{A_i A_j}}\right) \\ i \neq j \neq k,\end{aligned}\quad (29)$$

e.g., the  $j = 1$  component is

$$\begin{aligned}\frac{1}{p_1} \frac{\partial \tilde{H}}{\partial c_1} &= \sqrt{\frac{p_3}{p_1 p_2}} \sqrt{\frac{A_1 A_2}{A_3}} \cos\left(c_1 \sqrt{\frac{A_1}{A_2 A_3}}\right) \sin\left(c_3 \sqrt{\frac{A_3}{A_1 A_2}}\right) \\ &+ \sqrt{\frac{p_2}{p_1 p_3}} \sqrt{\frac{A_1 A_3}{A_2}} \cos\left(c_1 \sqrt{\frac{A_1}{A_2 A_3}}\right) \sin\left(c_2 \sqrt{\frac{A_2}{A_1 A_3}}\right).\end{aligned}$$

## 3. Shear

Finally, using (9) and (13), we find the following expression for the shear:

$$\begin{aligned}\sigma^2 &= \frac{(8\pi\gamma)^2}{3} \left[ \left( \frac{\partial H}{p_1 \partial c_1} - \frac{\partial H}{p_2 \partial c_2} \right)^2 + \left( \frac{\partial H}{p_2 \partial c_2} - \frac{\partial H}{p_3 \partial c_3} \right)^2 \right. \\ &\quad \left. + \left( \frac{\partial H}{p_3 \partial c_3} - \frac{\partial H}{p_1 \partial c_1} \right)^2 \right].\end{aligned}\quad (30)$$

## V. EFFECTIVE DYNAMICS: NUMERICAL STUDY

Here we address the effective dynamics of our model (25). In order to understand the choice of possible initial

conditions, we first briefly review the Bianchi I dynamics in GR.

### A. Initial conditions and Kasner indices

As it is well known (e.g., see [28]), when the classical Bianchi I geometry is sourced by a massless scalar field, the possible initial conditions for its associate Cauchy problem divide into the sets (of the starting points) of ‘‘Kasner-like’’ and ‘‘Kasner-unlike’’ solutions. Below we briefly review them following the notation of [27].

A straightforward computation reveals the vanishing of the following Poisson brackets:

$$\{p_\phi, \mathcal{C}_{gr}\}, \{p_i c_i, \mathcal{C}_{gr}\} \quad \forall i, \quad (31)$$

to which we associate the four constants of motion  $p_\phi, p_i c_i$ , which can be parametrized as

$$p_\phi := \sqrt{8\pi} \mathcal{K}_\phi, \quad p_i c_i := 8\pi\gamma \mathcal{K}_i \quad (32)$$

where  $\mathcal{K}_\phi := k k_\phi$ ,  $\mathcal{K}_i := k k_i$  and  $k$  a constant such that

$$k_1 + k_2 + k_3 = \pm 1. \quad (33)$$

The four real numbers  $\{k_\phi, k_i\}$  are called Kasner indices and in terms of them the vanishing of  $\mathcal{C}_{gr}$  reads

$$k_\phi^2 + k_1^2 + k_2^2 + k_3^2 = 1. \quad (34)$$

Without loss of generality, we can stick to the case  $\sum_i k_i = +1$  and  $k_\phi > 0$ . Kasner indices divide into two sets: the one where one  $k_i$  is negative and the other two are positive, which is called ‘‘Kasner-like’’, and the one where  $k_i > 0 \forall i$ , called ‘‘Kasner-unlike’’ (note that this set includes also the isotropic case  $k_i = 1/3$ ,  $i = 1, 2, 3$ ). Classically, for both sets the singularity is not avoided as it is clear from the general solution (35), which we give below for the scale factors (from which  $p_i(\phi)$  and  $c_i(\phi)$  can be immediately obtained using (5) and (15)):

$$a_i(\phi) = a_i(\phi_0) e^{\sqrt{8\pi} \frac{k_i}{k_\phi} (\phi - \phi_0)}. \quad (35)$$

In order to compare the dynamics provided by QRLG with the LQC one, we choose the same set of initial conditions for the Cauchy problem associated to the Hamilton's equations (9). This is a first order differential problem which admits a unique solution once seven initial conditions<sup>8</sup>  $\{p_i(0), c_i(0), p_\phi\}$  are chosen such that  $\mathcal{C}(p_i(0), c_i(0), p_\phi) = 0$ . To be sure that this common set fulfills (approximately) both the LQC and QRLG constraints (18), (25), we choose a set associated to a *classical* universe,

<sup>8</sup>For which we use a shorthand notation, e.g.,  $c_i(0) := c_i(\phi_0) = c_i(t_0)$ .

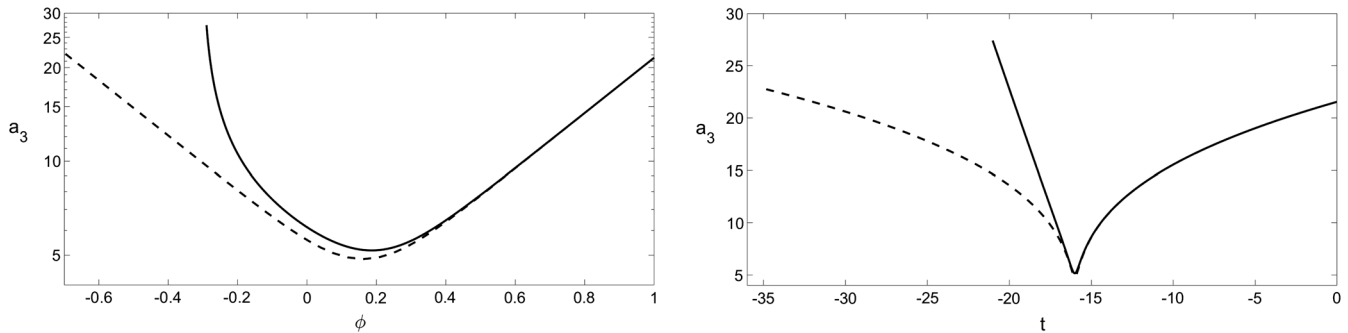


FIG. 1. Comparison between the QRLG dynamics (solid line) and the one provided by the LQC (dashed line) for isotropic initial conditions. Left panel:  $a_3$  vs the relational time  $\phi$ . Right panel:  $a_3$  vs the cosmological time  $t$ . In contrast to the LQC case, the QRLG evolution after the bounce is not longer Kasner like.

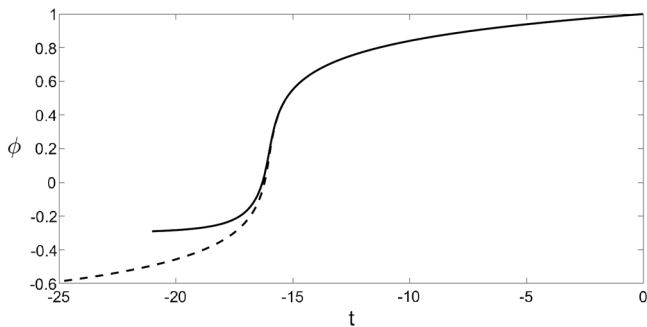


FIG. 2. Evolution of the field  $\phi$  vs  $t$  for the ISO case.

i.e.,  $p_i \gg 1$ ,  $c_i \ll 1$  ( $\mu_i c_i \ll 1$ ) where we know that the two constraints match. In this regime also GR holds and the possible initial conditions are those we were referring before, i.e., isotropic, Kasner-like and Kasner-unlike. For all these sets we follow the same strategy: we choose the same values of  $\{p_i(0), c_i(0)\}$  for both models and obtain  $p_{\phi\text{lqc}}$ ,  $p_{\phi\text{qrlg}}$  by imposing  $C_{\text{lqc}}(0) = 0$  and  $C_{\text{qrlg}}(0) = 0$ , respectively.

### B. The isotropic case (ISO)

The chosen initial conditions for the isotropic case are:  $p_i(0) = 10^{8/3}$ ,  $c_i(0) = 5 \times 10^{-5/3}$ ,  $p_{\phi\text{qrlg}} = 101.78960$ ,

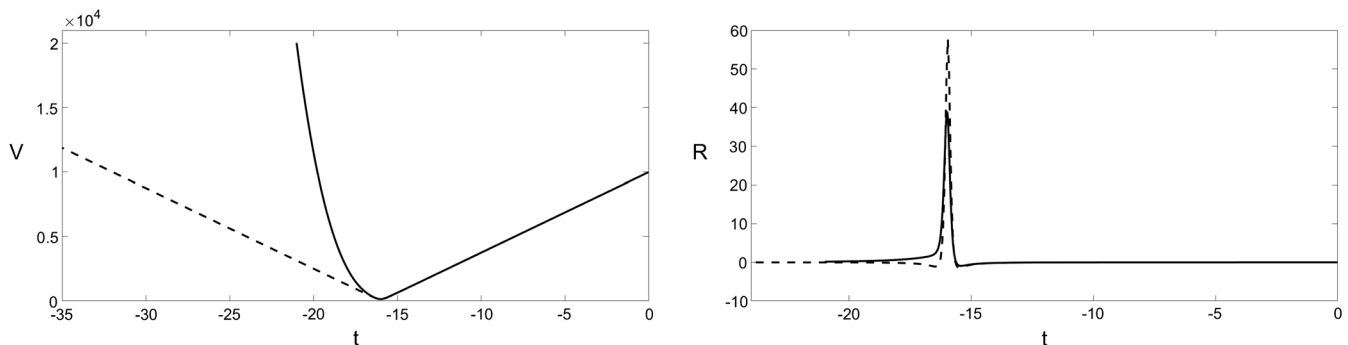


FIG. 3. Comparison between the QRLG (solid line) and the LQC (dashed line) dynamics for isotropic initial conditions. Left panel: the volume  $V$  vs the cosmological time  $t$ . Right panel: the scalar curvature  $R$  vs  $t$ . Similar behaviors are found for the KUL and KL cases.

and  $p_{\phi\text{lqc}} = 101.78998$ . In Fig. 1 we show the dynamics of the scale factor  $a_3$ , as it evolves in the relational time  $\phi$  and in the cosmological time  $t$  (the evolution along the other directions is exactly the same). After the bounce (which occurs approximately at the same time  $t_B = -16$ ,  $\phi_{B,\text{lqc}} \approx 0.16$ ,  $\phi_{B,\text{qrlg}} \approx 0.18$ ) the QRLG-Bianchi evolution shows a significant departure from the LQC one. In particular, looking at the left panel of Fig. 1, we see the two evolutions start differing from each other already a bit before the bounce.

For the QRLG model,  $\phi(t)$  approaches a constant value after the bounce time, i.e., for  $t < -16$  (see Fig. 2). This explains why the  $p_i(\phi)$  ( $a_i(\phi)$ ) have a faster evolution than the  $p_i(t)$  ( $a_i(t)$ ), indeed, as the field reaches the plateau the dynamics “accumulates” around  $\phi \approx -0.3$ . In particular, the scale factor grows linearly in time  $t$  (with slope  $-4.491$ ) after the bounce, explaining the vanishing behavior of the scalar curvature  $R$ ,

$$R = 2 \left( H_1 H_2 + H_2 H_3 + H_3 H_1 + \sum_i \frac{\ddot{a}_i}{a_i} \right), \quad (36)$$

in the far past (see the right panel of Fig. 3). As already observed in [27], the LQC evolution bridges two classical Bianchi I solutions, as it is clear from the dashed

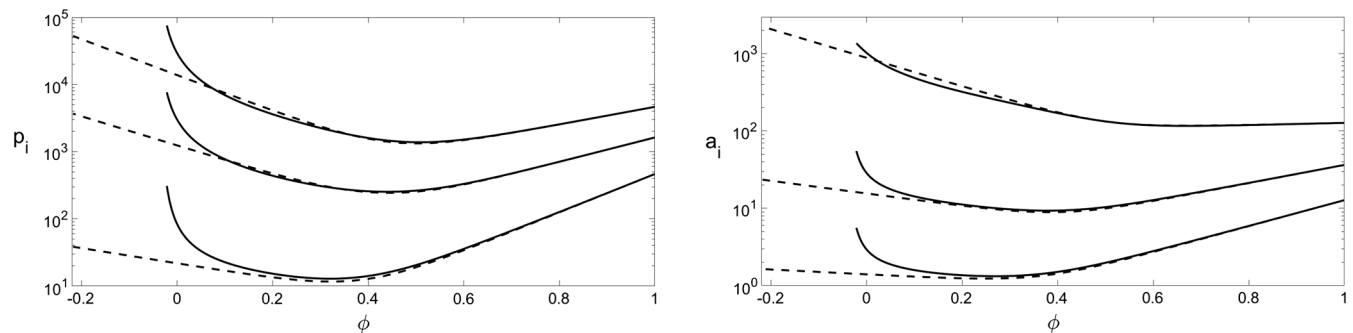


FIG. 4. Comparison between the QRLG (solid line) and the LQC (dashed line) dynamics for Kasner unlike initial conditions. Left panel from top to bottom:  $p_3, p_2, p_1$  vs the relational time  $\phi$ . Right panel from bottom to top: the scale factors  $a_3, a_2, a_1$  vs the relational time  $\phi$ . The Kasner indices for the LQC evolution are:  $k_1(0) = 0.0467, k_2(0) = 0.3925, k_3(0) = 0.5608$  and  $k_1 = -0.6203, k_2 = -0.2741, k_3 = -0.1056$ .

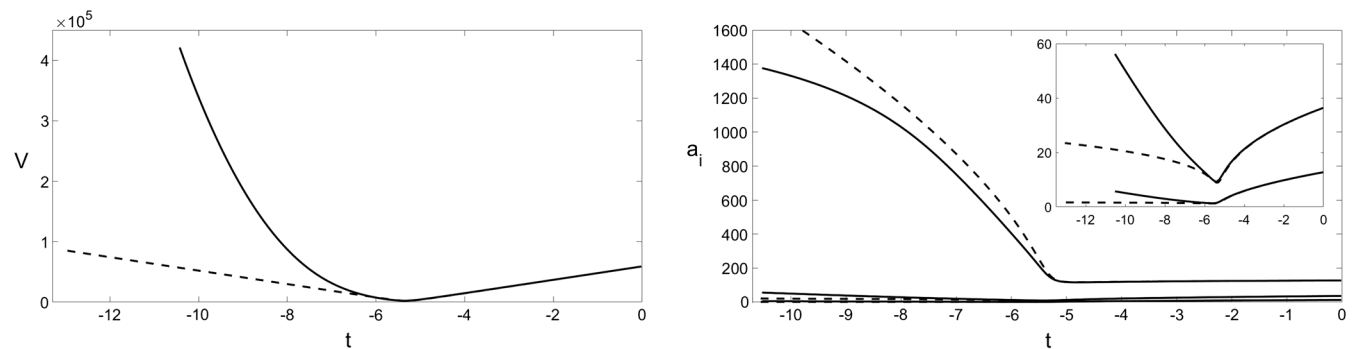


FIG. 5. Comparison between the QRLG (solid line) and the LQC (dashed line) dynamics for Kasner unlike initial conditions. Left panel:  $V$  vs  $t$ . Right panel from top to bottom: scale factors  $a_1, a_2, a_3$  vs the cosmological time  $t$ . The inset depicts the evolution of  $a_2$  and  $a_3$  vs  $t$ .

trajectories after and before the bounce in Fig. 1. This is not the case for the QRLG model, which is very peculiar. Going backwards in time, the QRLG Bianchi I universe starts as an initial classical Bianchi I and after the bounce undergoes an expansion that it is neither KL nor KUL, i.e., it never approaches the classical solution (35) for any Kasner index set. As we will see, this turns out to be a general feature of the QRLG dynamics, observed also in the evolutions associated to KUL and KL initial conditions (see Figs. 4, 6 and 7).

### C. The Kasner-unlike (KUL) case

Here we show the dynamics associated to the following anisotropic set of initial conditions:  $p_1(0) = 10^{8/3}, p_2(0) = 3.5 \times 10^{8/3}, p_3(0) = 10 \times 10^{8/3}, c_1(0) = 12.5 \times 10^{-5/3}, c_2(0) = 30 \times 10^{-5/3}, c_3(0) = 15 \times 10^{-5/3}, p_{\phi\text{lqc}} = 1616.8821$ , and  $p_{\phi\text{qrlg}} = 1616.7799$ . In Fig. 4 the physical areas<sup>9</sup>  $p_i$  and the scale factors  $a_i$  are plotted in the left and right panel, respectively. We see that the LQC model joins two classical Bianchi I universes associated to (initial) Kasner

indices  $k_i(0)$  and (final) Kasner indices  $k_i$ , such that<sup>10</sup>  $k_i = k_i(0) - 2/3$ . Instead, the QRLG evolution starts as a classical Bianchi I with  $k_i(0)$  like LQC but departs from the latter after the bounce and *accelerates* (going backwards in the relational time  $\phi$ ). In Fig. 5 the volume and the scale factors are plotted as they evolve in the cosmological time  $t$ , where the evolutions are power laws.

### D. The Kasner-like (KL) case

Finally, we present the anisotropic case associated to an initially contracting direction, e.g., to a negative  $c_2(0)$ . The chosen initial conditions for this case are  $p_1(0) = 4 \times 10^{8/3}, p_2(0) = 8 \times 10^{8/3}, p_3(0) = 3 \times 10^{8/3}, c_1(0) = 30 \times 10^{-5/3}, c_2(0) = -10^{-5/3}, c_3(0) = 20 \times 10^{-5/3}$ , and  $p_{\phi\text{qrlg}} = 891.9694, p_{\phi\text{lqc}} = 891.98209$ . Even though the evolutions of the areas  $p_i$  (showed in the left panel of Fig. 6) are similar to those of the KUL case, the scale factors (plotted in the right panel of the same figure) reveal a peculiar feature: each directional scale factor is non-vanishing, contrary to what we observe for the LQC model

<sup>9</sup>For which unitary fiducial lengths  $\bar{L}_i$  have been chosen.

<sup>10</sup>Confirming what already observed in [27].

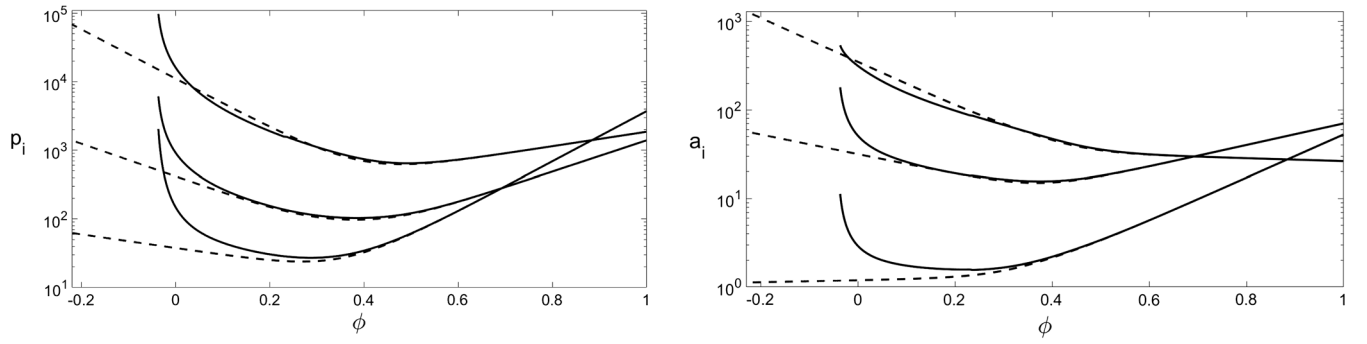


FIG. 6. Comparison between the dynamics of QRLG (solid line) and LQC (dashed line) for Kasner-like initial conditions. Left panel from top to bottom:  $p_1$ ,  $p_3$ ,  $p_2$  vs the relational time  $\phi$ . Right panel from top to bottom: evolution of the scale factors  $a_2$ ,  $a_3$ ,  $a_1$  vs the relational time  $\phi$ . The Kasner indices for the LQC evolution are:  $k_1(0) = 0.6978$ ,  $k_2(0) = -0.0465$ ,  $k_3(0) = 0.3488$  and  $k_1 = 0.0311$ ,  $k_2 = -0.7133$ ,  $k_3 = -0.3178$ . Note that the scale factors in the QRLG model are nonvanishing in *all* directions, contrarily to what happens in the LQC case where  $a_1$  goes to zero.

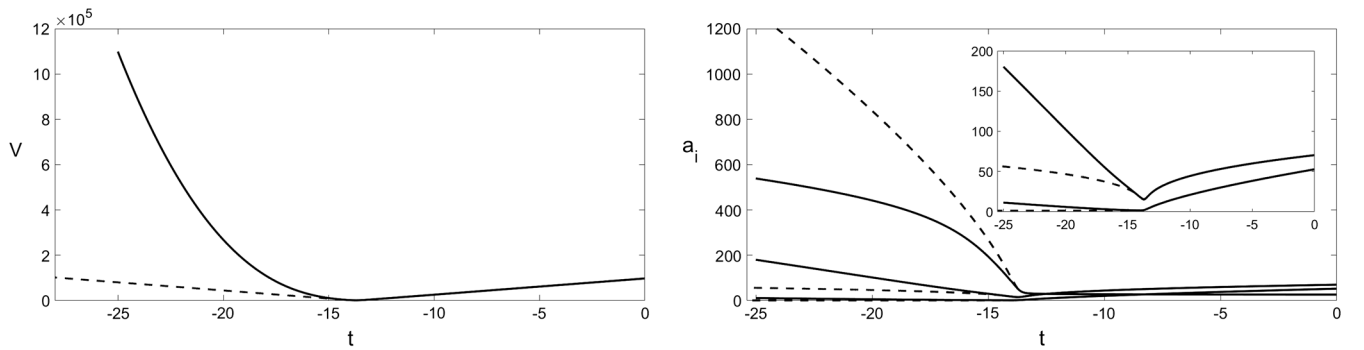


FIG. 7. Comparison between the dynamics of QRLG (solid line) and LQC (dashed line) for Kasner like initial conditions. Left panel:  $V$  vs  $t$ . Right panel from top to bottom: the evolution of the scale factors  $a_2$ ,  $a_3$ ,  $a_1$  vs  $t$ . The inset depicts the evolution of  $a_3$  and  $a_1$  vs  $t$ .

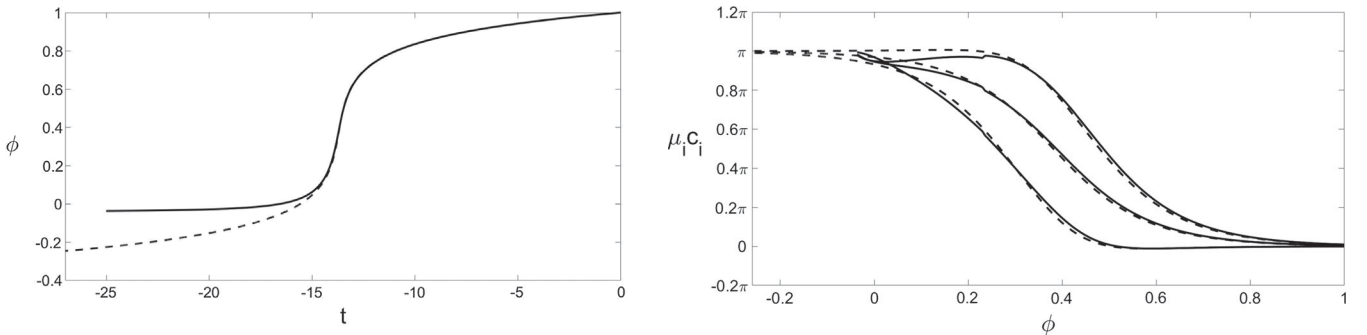


FIG. 8. Comparison between the dynamics of QRLG (solid line) and LQC (dashed line) for Kasner like initial conditions. Left panel: evolution of the field  $\phi$  vs the cosmological time  $t$ . Right panel from top to bottom: evolution of the semiclassical parameters  $\mu_1 c_1$ ,  $\mu_3 c_3$ ,  $\mu_2 c_2$  vs  $t$ , where  $\mu := \bar{\mu}, \mu'$ . Similar behaviors are obtained for the ISO and KUL cases.

where  $a_1$  goes to zero after its bounce (see the bottom dashed line in the right panel).

In closing, a natural question arises: why after the bounces the QRLG model does not follow a semiclassical Bianchi I evolution if its volume goes back to macroscopic values? A look at its Hamiltonian (24) is enough for the answer. Indeed, the QRLG Hamiltonian is an integral function whose next-to-the leading order contribution for

large volumes provide a first order correction to the Bianchi I LQC Hamiltonian that is proportional to the semiclassical parameter  $\mu'_i c_i$ , where  $\mu'_i := \sqrt{\Delta^3 p_i / (p_j p_k)}$ ,  $i \neq j \neq k$ . A straightforward computation reveals [6] that the ratio of this correction over the magnitude of a  $\sin^2$ -term in the LQC Hamiltonian (18) goes like  $V^{-2/3} \mu'_i c_i$ . Thus, for finite volumes  $V$ , both models match only when  $\mu'_i c_i \rightarrow 0$ . In the right panel of Fig. 8 we clearly see that this is no longer



TABLE I. Initial conditions for the three cases discussed in the main text.  $\alpha := 10^4$ ,  $\beta := 5 \times 10^{-3}$ .

Initial conditions					
ISO case		KUL case		KL case	
$p_1(0)$	$\alpha^{2/3}$	$p_1(0)$	$\alpha^{2/3}$	$p_1(0)$	$4\alpha^{2/3}$
$p_2(0)$	$\alpha^{2/3}$	$p_2(0)$	$3.5\alpha^{2/3}$	$p_2(0)$	$8\alpha^{2/3}$
$p_3(0)$	$\alpha^{2/3}$	$p_3(0)$	$10\alpha^{2/3}$	$p_3(0)$	$3\alpha^{2/3}$
$c_1(0)$	$\beta\alpha^{1/3}$	$c_1(0)$	$2.5\beta\alpha^{1/3}$	$c_1(0)$	$6\beta\alpha^{1/3}$
$c_2(0)$	$\beta\alpha^{1/3}$	$c_2(0)$	$6\beta\alpha^{1/3}$	$c_2(0)$	$-0.2\beta\alpha^{1/3}$
$c_3(0)$	$\beta\alpha^{1/3}$	$c_3(0)$	$3\beta\alpha^{1/3}$	$c_3(0)$	$4\beta\alpha^{1/3}$
$p_{\phi\text{qrlg}}$	101.789 60	$p_{\phi\text{qrlg}}$	1616.7799	$p_{\phi\text{qrlg}}$	891.969 40
$p_{\phi\text{lqc}}$	101.789 98	$p_{\phi\text{lqc}}$	1616.8821	$p_{\phi\text{lqc}}$	891.982 09

true for  $\phi \ll \phi_B \approx 0.3$ . For macroscopic times, the LQC evolution matches the GR one. The closer we are to  $\phi \approx \pi$  the better the LQC Hamiltonian is approximated by the classical one (14), but the QRLG model does not because its infinite contributions coming from the integral (24) are  $\mathcal{O}(1)$ .

### E. Technical details

Two strategies have been followed. On the one hand, we numerically solved the system of equations (9) by means of a fourth order Runge-Kutta Merson method in order to obtain  $p_2$ ,  $p_3$ ,  $c_1$ ,  $c_2$  and  $c_3$ , both for the QRLG and LQC model. In the first case,  $H$  of (7) is given by (24), while in the second case,  $H_{\text{lqc}}$  is provided by (18). On the other hand, we have obtained  $p_1$  directly from (7), which is regarded as an integral equation for  $p_1$ , by means of the Trust-Region Dogleg method implemented in the function `fsolve` of MATLAB® [29]. For the QRLG case, we evaluated the integrals by using the functions `integral1`, `integral2` and `integral3` encoded in MATLAB®, which make use of a global adaptive quadrature rule based on a Gauss-Kronrod scheme. We retained the default values for the absolute the relative tolerances, being  $10^{-10}$  and  $10^{-6}$  respectively. For the QRLG case, we have

chosen  $\Delta t = 0.0158$  for all the three cases analyzed, i.e., the ISO, KL, KUL case. As far as LQC concerns, we selected  $\Delta t = 0.05$  for both the ISO and KUL case, and  $\Delta t = 0.0016$  for the KL one, where the complete system of equations (9) have been solved to obtain  $p_1$  as well. The choice of the time step and the strategy of the solution are dictated by the necessity of keeping the  $C_{\text{qrlg}}$  of the order of at least  $10^{-8}$ , trying to minimize the computational time. The initial conditions of the simulations, together with the values of  $p_\phi$  used for QRLG and LQC are listed in Table I.

In Fig. 9 (left panel) we show the evolution of the  $C_{\text{qrlg}}$  vs  $t$  for the KL case. It can be seen that the values of  $C_{\text{qrlg}}$  are very low, precisely of the order of  $10^{-9}$  or less. However, we want to remark that the way we solved the dynamical problem always delivered small values of  $C_{\text{qrlg}}$ . This happens because  $p_1$  is computed directly from (25). In order to strengthen the reliability of our results, we compared the numerical solution obtained with this strategy with the one given by the solution of the complete system of equations (9), which does not depend on (25). We like to stress the fact that independently on the approach chosen to solve the problem, the dynamics must always be confined to the surface constraint within strict tolerances, i.e.,  $C_{\text{qrlg}} \approx 0$ . In case that the dynamics departs from the constraint surface,  $C_{\text{qrlg}}$  would strongly deviate from 0 with the second procedure. Therefore, a comparison between the numerical solutions of the governing equations obtained with the two strategies immediately indicates whether the solution computed with the first method is correct, since both solutions must match. Figure 9 (right panel) depicts the percentage of the relative difference of the volume computed with both strategies. It can be seen that the numerical results match well during the whole period of the evolution, with a maximum relative difference of approximately 2.7%. In addition, the numerical solution obtained by calculating  $p_1$  directly from (25) gives  $C_{\text{qrlg}}$  of the order of  $10^{-9}$  or less. Instead, the solution obtained by solving the complete system of equations (9) delivered  $C_{\text{qrlg}}$  of the order of  $10^{-4}$  with the chosen time step and

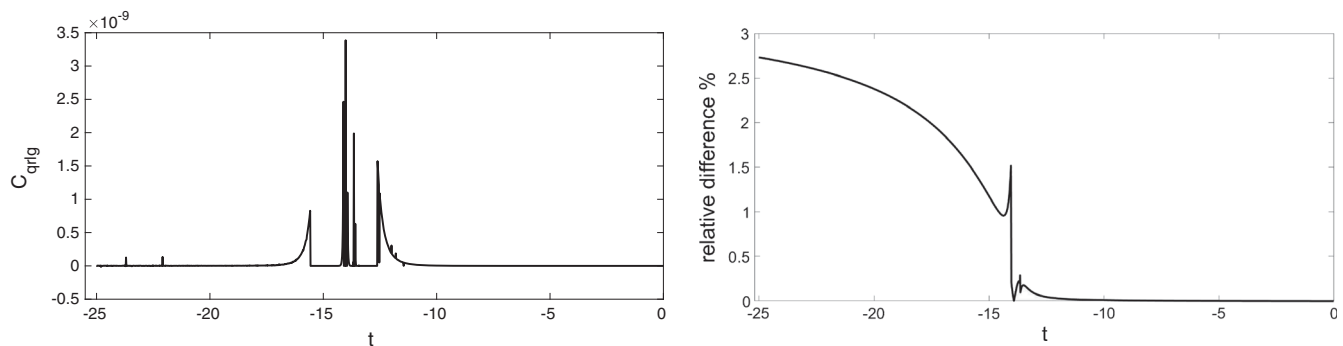


FIG. 9. Left panel: evolution of the  $C_{\text{qrlg}}$  vs  $t$  where  $p_1$  has been obtained from (25). Right panel: percentage of the relative difference of the volume obtained with the two methods vs  $t$ . In one case  $p_1$  is computed from (25) while in the other case  $p_1$  is computed from (9) together with  $p_2$ ,  $p_3$ ,  $c_1$ ,  $c_2$  and  $c_3$  by means of the fourth order Runge-Kutta-Merson method.

tolerances of the integrals. By utilizing this strategy for the QRLG case, the order of  $C_{\text{qrlg}}$  does not decrease significantly when the time step  $\Delta t$  is reduced. Thus, we have chosen to solve  $p_1$  from (25) in all the simulations for all the QRLG cases, even if the computational time required was higher, since the trust-region dogleg method is an iterative technique. This fact is more severe for the QRLG case, since numerical simulations required several days on a common workstation, while in the LQC case the computational time was just of the order of seconds.

## VI. ANALYTICAL UPPER BOUNDS FOR THE QRLG-BIANCHI I MODEL

Here we prove that energy density, expansion scalar and shear are bounded phase space functions along the effective dynamics provided by the QRLG constraint (22). To begin with, let us introduce the following quantity (where  $b := c/\sqrt{p}$ ):

$$H_{\text{disc},A}^{\text{FLRW}}(A^{\text{max}}(V), b) := -\frac{3}{8\pi\gamma^2} \left(\frac{\Delta' A^{\text{max}}}{2}\right)^{1/2} \frac{\sum_1^{A^{\text{max}}} \binom{A^{\text{max}}}{A} A \sin^2[b(\frac{\Delta' A^{\text{max}}}{2A})^{1/2}]}{\sum_1^{A^{\text{max}}} \binom{A^{\text{max}}}{A}}, \quad (37)$$

which is the effective QRLG-Hamiltonian for the FLRW model, as provided by the (area counting) statistical regularization scheme [6]. In order to show the boundness of the energy density  $\rho^{\text{disc}}$  for the QRLG-Bianchi I model, i.e., of (26) with Gaussians replaced by binomials as in (22), we will use as a preliminary lemma the boundness of the energy density associated to (37), which we prove below.

### A. Energy density upper bound for the QRLG-FLRW model

The energy density for the FLRW model is given by the ratio of (37) over the volume  $V = (\Delta' A^{\text{max}}/2)^{3/2}$  [6], followed by a sign change, i.e.,

$$\rho_{\text{disc},A}^{\text{FLRW}} = \frac{3}{8\pi\gamma^2} \left(\frac{\Delta' A^{\text{max}}}{2}\right)^{-1} \frac{1}{2^{A^{\text{max}}}-1} \sum_1^{A^{\text{max}}} \binom{A^{\text{max}}}{A} \times A \sin^2 \left[ b \left(\frac{\Delta' A^{\text{max}}}{2A}\right)^{1/2} \right] \quad (38)$$

where we have used

$$\sum_1^{A^{\text{max}}} \binom{A^{\text{max}}}{A} = 2^{A^{\text{max}}} - 1. \quad (39)$$

Clearly, the following holds:

$$\rho_{\text{disc},A}^{\text{FLRW}} \leq \frac{3}{8\pi\gamma^2} \left(\frac{\Delta' A^{\text{max}}}{2}\right)^{-1} \frac{1}{2^{A^{\text{max}}}-1} \sum_1^{A^{\text{max}}} \binom{A^{\text{max}}}{A} A \quad (40)$$

and using

$$\sum_1^{A^{\text{max}}} \binom{A^{\text{max}}}{A} A = A^{\text{max}} 2^{A^{\text{max}}-1}, \quad (41)$$

we find

$$\rho_{\text{disc},A}^{\text{FLRW}} \leq \frac{3}{4\Delta'\pi\gamma^2} \max_{A_1^{\text{max}} \geq 1} S(A^{\text{max}}), \quad (42)$$

having called

$$S(A^{\text{max}}) := \frac{2^{A^{\text{max}}}-1}{2^{A^{\text{max}}}-1}, \quad (43)$$

which is a decreasing monotonic sequence whose maximum value is 1, reached at  $A^{\text{max}} = 1$ . Thus, we end up with the following upper bound:

$$\rho_{\text{disc},A}^{\text{FLRW}} \leq \frac{3}{4\Delta'\pi\gamma^2}. \quad (44)$$

### B. Energy density upper bound for the QRLG-Bianchi I model

For Bianchi I we use expression (22), change its sign and divide it by the volume

$$V = \sqrt{p_1 p_2 p_3} = \left(\frac{\Delta'}{2}\right)^{3/2} \sqrt{A_1^{\text{max}} A_2^{\text{max}} A_3^{\text{max}}}.$$

Proceeding analogously to the QRLG-FLRW case, we arrive at the following inequality for the QRLG-Bianchi I energy density:

$$\rho \leq \frac{1}{4\Delta'\pi\gamma^2} 3 \max_{A_1^{\text{max}} \geq 1} S(A_1^{\text{max}}), \quad (45)$$

where  $S$  is the sequence (43). Thus, we find the same bound we had for the isotropic case, i.e.,

$$\rho \leq \frac{3}{4\Delta'\pi\gamma^2} = 0.6874. \quad (46)$$

### C. Expansion scalar and shear upper bounds

For the sake of clarity, here we start working within the continuous approximation. In order to show the boundness of  $\theta$  and  $\sigma^2$ , it is enough to find an upper bound for the term

$\frac{\partial H}{p_j \partial c_j}$ , as it is clear from expressions (27) and (30). From the definitions (24) and (29), it follows that

$$\left| \frac{\partial H}{p_j \partial c_j} \right| \leq \frac{1}{8\pi\gamma^2} \sum_{i,k} \sqrt{\frac{p_k}{p_j p_i}} \frac{\left[ \prod_i \int_1^{2p_i/\Delta'} e^{-\frac{\Delta'}{p_i}(A_i - \frac{p_i}{\Delta'})^2} dA_i \right] \sqrt{\frac{A_j A_i}{A_k}}}{\prod_i \int_1^{2p_i/\Delta'} e^{-\frac{\Delta'}{p_i}(A_i - \frac{p_i}{\Delta'})^2} dA_i} \quad (47)$$

$i \neq j \neq k.$

For any given  $j$ , the r.h.s. is a sum of two terms which is symmetric under  $k \leftrightarrow i$ , e.g., for  $j = 1$  we have

$$\left| \frac{\partial H}{p_1 \partial c_1} \right| \leq \frac{1}{8\pi\gamma^2} [I_1(p_1)I_2(p_2)I_1(p_3) + I_1(p_1)I_2(p_3)I_1(p_2)]$$

where

$$I_1(p_1) := \frac{1}{\sqrt{p_1}} \frac{\int_1^{2p_1/\Delta'} e^{-\frac{\Delta'}{p_1}(A_1 - \frac{p_1}{\Delta'})^2} \sqrt{A_1} dA_1}{\int_1^{2p_1/\Delta'} e^{-\frac{\Delta'}{p_1}(A_1 - \frac{p_1}{\Delta'})^2} dA_1}, \quad (48)$$

$$I_2(p_2) := \sqrt{p_2} \frac{\int_1^{2p_2/\Delta'} e^{-\frac{\Delta'}{p_2}(A_2 - \frac{p_2}{\Delta'})^2} \frac{1}{\sqrt{A_2}} dA_2}{\int_1^{2p_2/\Delta'} e^{-\frac{\Delta'}{p_2}(A_2 - \frac{p_2}{\Delta'})^2} dA_2}. \quad (49)$$

$I_1$  and  $I_2$  are integral functions whose inspection at their boundaries is enough to understand whether they are bounded or not. Their asymptotic behavior as  $p_i \rightarrow \infty$  may be obtained with the Laplace method:

$$\lim_{p_1 \rightarrow \infty} I_1(p_1) = \frac{1}{\sqrt{\Delta'}}, \quad \lim_{p_2 \rightarrow \infty} I_2(p_2) = \sqrt{\Delta'}. \quad (50)$$

Still, the limits at  $p_i = \frac{\Delta'}{2}$  remain. At those points the continuous approximation (24) is no longer reliable (*a priori*) and the exact definition (22) must be taken into account, which implies the inspection of the discrete versions of functions  $I_1$  and  $I_2$ , i.e.,

$$I_1^{\text{disc}}(A_1^{\text{max}}) := \frac{\sqrt{2}}{\sqrt{A_1^{\text{max}} \Delta'} (2^{A_1^{\text{max}}} - 1)} \sum_1^{A_1^{\text{max}}} \binom{A_1^{\text{max}}}{A_1} \sqrt{A_1}, \quad (51)$$

$$I_2^{\text{disc}}(A_2^{\text{max}}) := \frac{\sqrt{A_2^{\text{max}} \Delta'}}{\sqrt{2} (2^{A_2^{\text{max}}} - 1)} \sum_1^{A_2^{\text{max}}} \binom{A_2^{\text{max}}}{A_2} \frac{1}{\sqrt{A_2}}, \quad (52)$$

where we have used (20) and (39). The sequences  $I_1^{\text{disc}}(A_1^{\text{max}})$  and  $I_2^{\text{disc}}(A_2^{\text{max}})$  are plotted in Figs. 10 and 11 together with their continuous approximations (48), (49), from which we easily read their maximum values:  $\max(I_1^{\text{disc}}) = 0.576 = 1.414/\sqrt{\Delta'}$  and  $\max(I_2^{\text{disc}}) = 2.616 = 1.065\sqrt{\Delta'}$ .

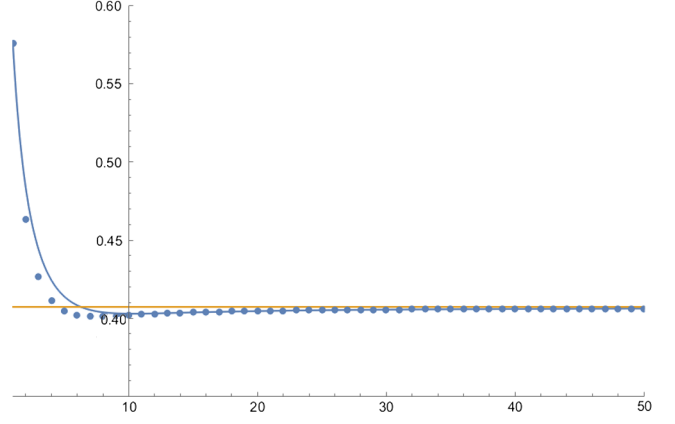


FIG. 10. The sequence  $I_1^{\text{disc}}(A_1^{\text{max}})$  and its continuous approximation  $I_1(A_1^{\text{max}})$  defined in the text, together with their common asymptote  $I_1 = 1/\sqrt{\Delta'}$ . The maximum value of  $I_1^{\text{disc}}$  is 0.576, reached at  $A_1^{\text{max}} = 1$ . Note the sequence starts matching its continuous approximation already for  $A_1^{\text{max}} > 10$ .

Thus,

$$\left| \frac{\partial H}{p_j \partial c_j} \right| \leq \frac{1}{8\pi\gamma^2} 2[\max_{A_1^{\text{max}} \geq 1} I_1^{\text{disc}}(A_1^{\text{max}})]^2 \max_{A_2^{\text{max}} \geq 1} I_2^{\text{disc}}(A_2^{\text{max}}) = \frac{2.129}{\sqrt{\Delta'} 4\pi\gamma^2}. \quad (53)$$

From definition (27) we find the following upper bound for the absolute value of the expansion scalar:

$$|\theta| \leq 3 \frac{8\pi\gamma}{2} \frac{2.129}{\sqrt{\Delta'} 4\pi\gamma^2} = \frac{6.387}{\sqrt{\Delta'} \gamma} = 10.8375, \quad (54)$$

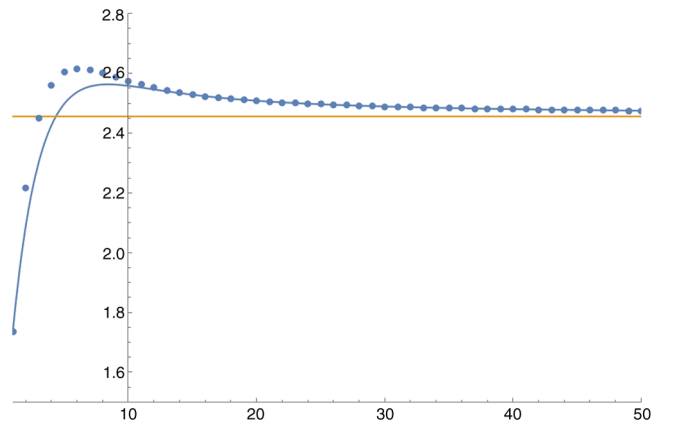


FIG. 11. The sequence  $I_2^{\text{disc}}(A_2^{\text{max}})$  and its continuous approximation  $I_2(A_2^{\text{max}})$  defined in the text, together with their common asymptote  $I_2 = \sqrt{\Delta'}$ . The maximum value of  $I_2^{\text{disc}}$  is 2.616 reached at  $A_2^{\text{max}} = 6$  (the relative difference with the maximum of  $I_2$  is only around 2%). Note the sequence starts matching its continuous approximation already for  $A_2^{\text{max}} > 12$ .

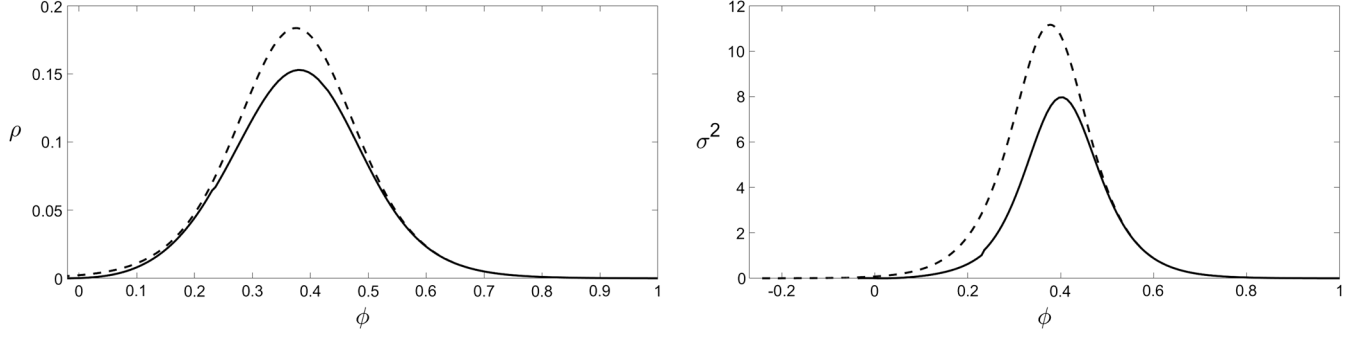


FIG. 12. Comparison between the QRLG (solid line) and the LQC (dashed line) model for Kasner-like initial conditions. Left panel: evolution of the energy density  $\rho$  vs  $\phi$ . Right panel: evolution of the shear  $\sigma^2$  vs  $\phi$ . The maximum and the minimum values are:  $\rho_{\text{QRLG}}^{\text{max}} = 0.1529$ ,  $\rho_{\text{LQC}}^{\text{max}} = 0.1837$ ,  $\sigma_{\text{QRLG}}^2{}^{\text{max}} = 7.9670$ , and  $\sigma_{\text{LQC}}^2{}^{\text{max}} = 11.1605$ .

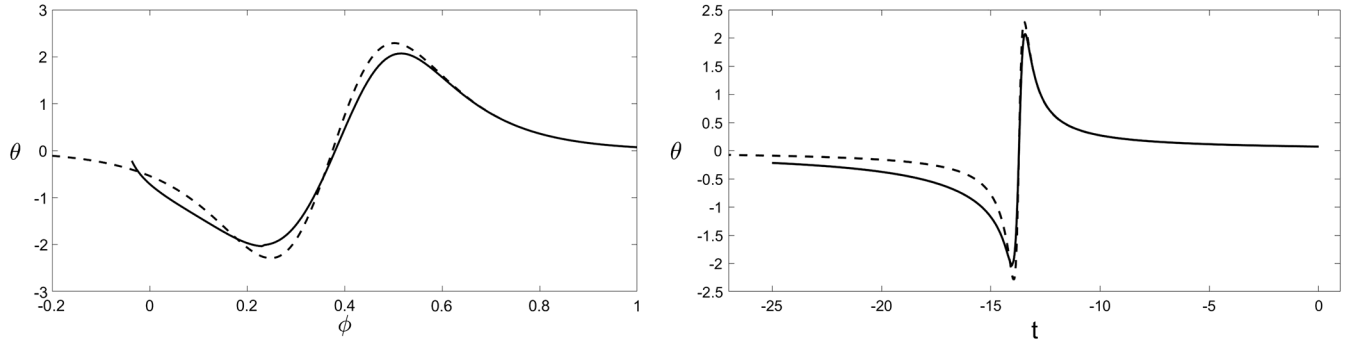


FIG. 13. Comparison between the QRLG (solid line) and the LQC (dashed line) model for Kasner-like initial conditions. Left panel: evolution of the expansion scalar  $\theta$  vs  $\phi$ . Right panel: evolution of the expansion scalar  $\theta$  vs  $t$ . The maximum and the minimum values are:  $\theta_{\text{QRLG}}^{\text{max}} = 2.0712$ ,  $\theta_{\text{LQC}}^{\text{max}} = 2.2909$ ,  $\theta_{\text{QRLG}}^{\text{min}} = -2.0368$ , and  $\theta_{\text{LQC}}^{\text{min}} = -2.2909$ .

from (30), the upper bound for the shear is found to be

$$\begin{aligned} \sigma^2 &\leq 3 \frac{(8\pi\gamma)^2}{3} \left( 2 \max_{A^{\text{max}} \geq 1} \left| \frac{\partial H}{p_j \partial c_j} \right| \right)^2 \\ &= \frac{72.522}{\Delta'\gamma^2} = 208.7998. \end{aligned} \quad (55)$$

#### D. $\rho$ , $\theta$ and $\sigma^2$ along physical motions

Here we show the numerical evolutions of the quantities  $\rho$ ,  $\theta$ , and  $\sigma^2$  along the physical motion (see Figs. 12 and 13) associated to the KL set of initial conditions discussed before (see Table I). Their maxima are reported in the captions and they all respect the analytical bounds (46), (54) and (55). ISO and KUL cases provide similar plots, therefore we do not show them here. In particular, in the QRLG model all the quantities turn out to reach a maximum value that is significantly smaller than the one reached in LQC. Their maximum relative difference between the two models  $\Delta\rho := |\rho_{\text{LQC}} - \rho_{\text{QRLG}}|/\rho_{\text{LQC}}$ ,  $\Delta\theta := |\theta_{\text{LQC}} - \theta_{\text{QRLG}}|/\theta_{\text{LQC}}$ ,  $\Delta\sigma^2 := |\sigma_{\text{LQC}}^2 - \sigma_{\text{QRLG}}^2|/\sigma_{\text{LQC}}^2$  are 16.76%, 11.09% and 28.61%, respectively.

Finally, note the evolution of  $\theta$  in the relational time  $\phi$  (left panel of Fig. 13) is consistent with the dynamics of  $\phi$ , plotted in the left panel of Fig. 8. Indeed, as we approach  $\phi = -0.0365$ ,  $d\phi/dt \approx 0$  and thus  $d\theta/d\phi \equiv (d\theta/dt)(d\phi/dt)^{-1}$  speeds up as observed. Moreover, the ‘‘accumulation point’’  $\phi = -0.0365$  is reached for  $t \rightarrow -\infty$  and there is no chance for  $\theta$  to grow more than what observed in Fig. 13.

## VII. CONCLUSIONS

Since a complete theory of quantum gravity is still lacking, insights about the Planck-scale physics rely on several different approaches, such as the one pursued by string theory [30,31], LQG [3,4], and non-commutative geometry [32], only to cite a few. Even within a given approach, mathematical ambiguities can arise when the machinery of a given theory is applied to a symmetry reduced system to perform computations. This is the case of LQG, where several possible models for the description of our primordial universe come from its covariant [33–35], canonical [6,12,36] and group field theory [37] formulation.

In this paper we have studied an anisotropic, homogeneous model for the quantum cosmology of Bianchi I geometry in LQG within the QRLG framework and compared it with effective LQC. The numerical simulations of the evolution of the LQC-Bianchi I and the QRLG-Bianchi I model have all been run starting from (approximately) common initial conditions that correspond to a classical Bianchi I universe. The LQC evolution is observed to bridge two classical Bianchi I universes before and after the bounces, in agreement with [27], whereas this does not happen for the QRLG-model. Going backwards in the relational time  $\phi$ , the QRLG evolution starts departing from the LQC one already a bit before the bounces. Those occur only once in each direction, and then an accelerated evolution of each scale factor is observed. The main result is that the QRLG dynamics resolves the classical singularity for *all* kind of initial conditions. In particular, the scale factors turn out to vanish in *all* directions, contrary to what happens in LQC. In the latter case, one of the scale factor turns out to be vanishing in the far past for Kasner-like initial conditions, confirming what already observed in [27]. The simulations have been done for three different kinds of classical initial conditions, namely the isotropic, Kasner-like and Kasner-unlike ones. The reliability on the observed singularity resolution in QRLG is strengthened by the analytical upper bounds we have found for the energy density, expansion scalar and shear.

Another difference between the QRLG-model and the LQC one is that for isotropic initial conditions, the former does not reduce to the QRLG-FLRW model, i.e., to the emergent bouncing universe [5,6]. Instead, a LQC-Bianchi I reduces to a LQC-FLRW. This is clear from the mathematical point of view, since a dynamics that starts with isotropic conditions keep evolving isotropically and since the QRLG-Bianchi I Hamiltonian does not reduce to the QRLG-FLRW one in the isotropic limit  $p_i \rightarrow p$ ,  $c_i \rightarrow c$ . Therefore, the isotropic dynamics of the QRLG-Bianchi I must differ from the ones of the QRLG-FLRW, as observed. Thus, contrary to

what happens for LQC, the prebounce phenomenological traces of a QRLG primordial universe could be used in principle to understand whether the late (isotropic) universe comes from the isotropic QRLG-Bianchi I model or the QRLG-FLRW one.

A comparison between the isotropic QRLG-Bianchi I and the recently introduced Dapor-Liegener model [36] comes natural, since both show a departure from standard LQC before the bounce. Backwards in the cosmological time  $t$ , the latter describes an isotropic universe that starts as a contracting classical FLRW, undergoes a bounce and expands forever according to a non-Friedmanian evolution whose limit in the far past is exponential, i.e., driven by a Planckian valued cosmological constant. Thus, both the QRLG-Bianchi I and the Dapor-Liegener model do not exit the quantum regime after the bounce but while the latter here expands exponentially, the former does it only linearly.

In closing, our study has shown that QRLG offers a viable alternative to the standard picture drawn by LQC, providing a singularity-free model for anisotropic cosmology. Investigations both in the phenomenological and theoretical side remain to be done in the near future, such as computing the power spectrum of tensor and scalar perturbations propagating on the QRLG-Bianchi I effective background, and addressing the quantum dynamics by using a graph-changing Hamiltonian operator. The former will (hopefully) provide crucial observable predictions for testing the effective scenario and the latter deeper insights on QRLG-quantum dynamics beyond its effective scheme.

## ACKNOWLEDGMENTS

This work was supported in part by the NSF Grant No. PHY-1505411, the Eberly research funds of Penn State. G. B. would like to thank the Grant No. 2018/29/B/ST2/01250 of the Polish Narodowe Centrum Nauki.

- 
- [1] E. Alesci and F. Cianfrani, Quantum-reduced loop gravity: Cosmology, *Phys. Rev. D* **87**, 083521 (2013).
  - [2] E. Alesci and F. Cianfrani, Quantum reduced loop gravity and the foundation of loop quantum cosmology, *Int. J. Mod. Phys. D* **25**, 1642005 (2016).
  - [3] C. Rovelli, *Quantum Gravity*, Cambridge Monographs on Mathematical Physics (Cambridge University Press, Cambridge, England, 2004).
  - [4] T. Thiemann, *Modern Canonical Quantum General Relativity* (Cambridge University Press, Cambridge, England, 2008).
  - [5] E. Alesci, G. Botta, F. Cianfrani, and S. Liberati, Cosmological singularity resolution from quantum gravity: The emergent-bouncing universe, *Phys. Rev. D* **96**, 046008 (2017).
  - [6] E. Alesci, G. Botta, and G. V. Stagno, Quantum reduced loop gravity effective Hamiltonians from a statistical regularization scheme, *Phys. Rev. D* **97**, 046011 (2018).
  - [7] E. Alesci, S. Bahrami, and D. Pranzetti, Quantum evolution of black hole initial data sets: Foundations, *Phys. Rev. D* **98**, 046014 (2018).
  - [8] E. Alesci, C. Pacilio, and D. Pranzetti, Orthogonal gauge fixing of first order gravity, *Phys. Rev. D* **98**, 044052 (2018).
  - [9] E. Alesci and F. Cianfrani, Quantum reduced loop gravity: Semiclassical limit, *Phys. Rev. D* **90**, 024006 (2014).

- [10] E. Alesci and F. Cianfrani, Improved regularization from quantum reduced loop gravity, [arXiv:1604.02375](#).
- [11] E. Alesci, A. Barrau, G. Botta, K. Martineau, and G. Stagno, Phenomenology of quantum reduced loop gravity in the isotropic cosmological sector, *Phys. Rev. D* **98**, 106022 (2018).
- [12] I. Agullo and P. Singh, *Loop Quantum Cosmology*, edited by A. Ashtekar and J. Pullin, *Loop Quantum Gravity: The First 30 Years* (World scientific, 2017), pp. 183–240.
- [13] E. Alesci and F. Cianfrani, Loop quantum cosmology from quantum reduced loop gravity, *Europhys. Lett.* **111**, 40002 (2015).
- [14] A. Ashtekar, T. Pawłowski, and P. Singh, Quantum nature of the big bang: Improved dynamics, *Phys. Rev. D* **74**, 084003 (2006).
- [15] R. Brandenberger, Q. Liang, R. O. Ramos, and S. Zhou, Fluctuations through a vibrating bounce, *Phys. Rev. D* **97**, 043504 (2018).
- [16] K. Martineau and A. Barrau, Primordial power spectra from an emergent universe: Basic results and clarifications, *Universe* **4**, 149 (2018).
- [17] J. Olmedo and E. Alesci, Power spectrum of primordial perturbations for an emergent universe in quantum reduced loop gravity, [arXiv:1811.04327](#).
- [18] F. Cianfrani, G. Montani, and M. Muccino, Semi-classical isotropization of the universe during a de Sitter phase, *Phys. Rev. D* **82**, 103524 (2010).
- [19] D.-W. Chiou, Loop quantum cosmology in Bianchi type I models: Analytical investigation, *Phys. Rev. D* **75**, 024029 (2007).
- [20] D.-W. Chiou and K. Vandersloot, Behavior of nonlinear anisotropies in bouncing Bianchi I models of loop quantum cosmology, *Phys. Rev. D* **76**, 084015 (2007).
- [21] L. Szulc, Loop quantum cosmology of diagonal Bianchi type I model: Simplifications and scaling problems, *Phys. Rev. D* **78**, 064035 (2008).
- [22] A. Corichi and P. Singh, Geometric perspective on singularity resolution and uniqueness in loop quantum cosmology, *Phys. Rev. D* **80**, 044024 (2009).
- [23] M. Bojowald, D. Cartin, and G. Khanna, Lattice refining loop quantum cosmology, anisotropic models, and stability, *Phys. Rev. D* **76**, 064018 (2007).
- [24] A. Ashtekar, M. Bojowald, and J. Lewandowski, Mathematical structure of loop quantum cosmology, *Adv. Theor. Math. Phys.* **7**, 233 (2003).
- [25] A. Ashtekar and E. Wilson-Ewing, Loop quantum cosmology of Bianchi I models, *Phys. Rev. D* **79**, 083535 (2009).
- [26] N. Bodendorfer, Quantum reduction to Bianchi I models in loop quantum gravity, *Phys. Rev. D* **91**, 081502 (2015).
- [27] D.-W. Chiou, Effective dynamics, big bounces and scaling symmetry in Bianchi type I loop quantum cosmology, *Phys. Rev. D* **76**, 124037 (2007).
- [28] G. Montani, M. V. Battisti, R. Benini, and G. Imponente, *Primordial Cosmology* (World Scientific, Singapore, 2009).
- [29] M. J. D. Powell, *A Fortran Subroutine for Solving Systems of Nonlinear Algebraic Equations*, edited by P. Rabinowitz, *Numerical Methods for Nonlinear Algebraic Equations* (Gordon & Breach, London, UK, 1970), pp. 87–114.
- [30] J. Polchinski, *String Theory, Vol. 1: An Introduction to the Bosonic String*, Cambridge Monographs on Mathematical Physics (Cambridge University Press, Cambridge, England, 2007).
- [31] J. Polchinski, *String Theory. Vol. 2: Superstring Theory and Beyond*, Cambridge Monographs on Mathematical Physics (Cambridge University Press, Cambridge, England, 2007).
- [32] A. Connes, A short survey of noncommutative geometry, *J. Math. Phys. (N.Y.)* **41**, 3832 (2000).
- [33] E. Bianchi, C. Rovelli, and F. Vidotto, Towards Spinfoam Cosmology, *Phys. Rev. D* **82**, 084035 (2010).
- [34] M. Kisielowski, J. Lewandowski, and J. Puchta, One vertex spin-foams with the dipole cosmology boundary, *Classical Quantum Gravity* **30**, 025007 (2013).
- [35] G. Sarno, S. Speziale, and G. V. Stagno, 2-vertex Lorentzian spin foam amplitudes for dipole transitions, *Gen. Relativ. Gravit.* **50**, 43 (2018).
- [36] A. Dapor and K. Liegener, Cosmological effective hamiltonian from full loop quantum gravity dynamics, *Phys. Lett. B* **785**, 506 (2018).
- [37] S. Gielen and L. Sindoni, Quantum cosmology from group field theory condensates: A review, *SIGMA* **12**, 082 (2016).